

A Dynamical Investigation of the May 2004 McMurdo Antarctica Severe Wind Event Using AMPS*

DANIEL F. STEINHOFF, DAVID H. BROMWICH, AND MICHELLE LAMBERTSON

Polar Meteorology Group, Byrd Polar Research Center, and Atmospheric Sciences Program, Department of Geography, The Ohio State University, Columbus, Ohio

SHELLEY L. KNUTH AND MATTHEW A. LAZZARA

Antarctic Meteorological Research Center, Space Science and Engineering Center, University of Wisconsin—Madison, Madison, Wisconsin

(Manuscript received 21 August 2006, in final form 12 April 2007)

ABSTRACT

On 15–16 May 2004 a severe windstorm struck McMurdo, Antarctica. The Antarctic Mesoscale Prediction System (AMPS) is used, along with available observations, to analyze the storm. A synoptic-scale cyclone weakens as it propagates across the Ross Ice Shelf toward McMurdo. Flow associated with the cyclone initiates a barrier jet along the Transantarctic Mountains. Forcing terms from the horizontal equations of motion are computed in the barrier wind to show that the local time tendency and momentum advection terms are key components of the force balance. The barrier jet interacts with a preexisting near-surface radiation inversion over the Ross Ice Shelf to set up conditions favorable for the development of large-amplitude mountain waves, leading to a downslope windstorm in the Ross Island area. Hydraulic theory can explain the structure of the downslope windstorms, with amplification of the mountain waves possibly caused by wave-breaking events. The underestimation of AMPS wind speed at McMurdo is caused by the misplacement of a hydraulic jump downstream of the downslope windstorms. The dynamics associated with the cyclone, barrier jet, and downslope windstorms are analyzed to determine the role of each in development of the severe winds.

1. Introduction

During 15–16 May 2004, a severe windstorm struck McMurdo Station, Antarctica. Official observations are lacking because the anemometer was blown away; however, observations from McMurdo Building 71 recorded a maximum wind speed of 71.5 m s^{-1} and sustained wind speeds of $35\text{--}50 \text{ m s}^{-1}$ between 1800 UTC 15 May and 0000 UTC 16 May (Dalrymple 2004). Observations from nearby Arrival Heights and Black Island recorded maximum speeds of 84 and 64 m s^{-1} , respectively, and sustained winds of 35 and 48 m s^{-1} ,

respectively, during the same time period. McMurdo Station suffered structural damage to buildings and vehicles [see Dalrymple (2004) for more detailed damage description], as did neighboring Scott Base (New Zealand).

Figure 1 features a series of maps designed to familiarize the reader with Antarctic geography and station locations on the Ross Ice Shelf and in the McMurdo area. Climatologically, the strongest wind regimes in Antarctica are located along steep coastal slopes, such as Cape Denison, which is associated with the broad-scale convergence of katabatic flow from the continental interior to a restricted coastal zone (Schwerdtfeger 1984). Katabatic effects occasionally reach McMurdo directly from Siple Coast (Bromwich et al. 1992) and sources along the Transantarctic Mountains (Liu and Bromwich 1993). For this case, the complex topography of the region (Figs. 1b,c) modifies preexisting synoptic-scale and mesoscale features to produce wind speeds rivaling those found in the strongest katabatic zones.

* Byrd Polar Research Center Contribution Number 1350.

Corresponding author address: Daniel F. Steinhoff, Polar Meteorology Group, Byrd Polar Research Center, The Ohio State University, 1090 Carmack Road, Columbus, OH 43210.
E-mail: steinhoff@polarmet1.mps.ohio-state.edu

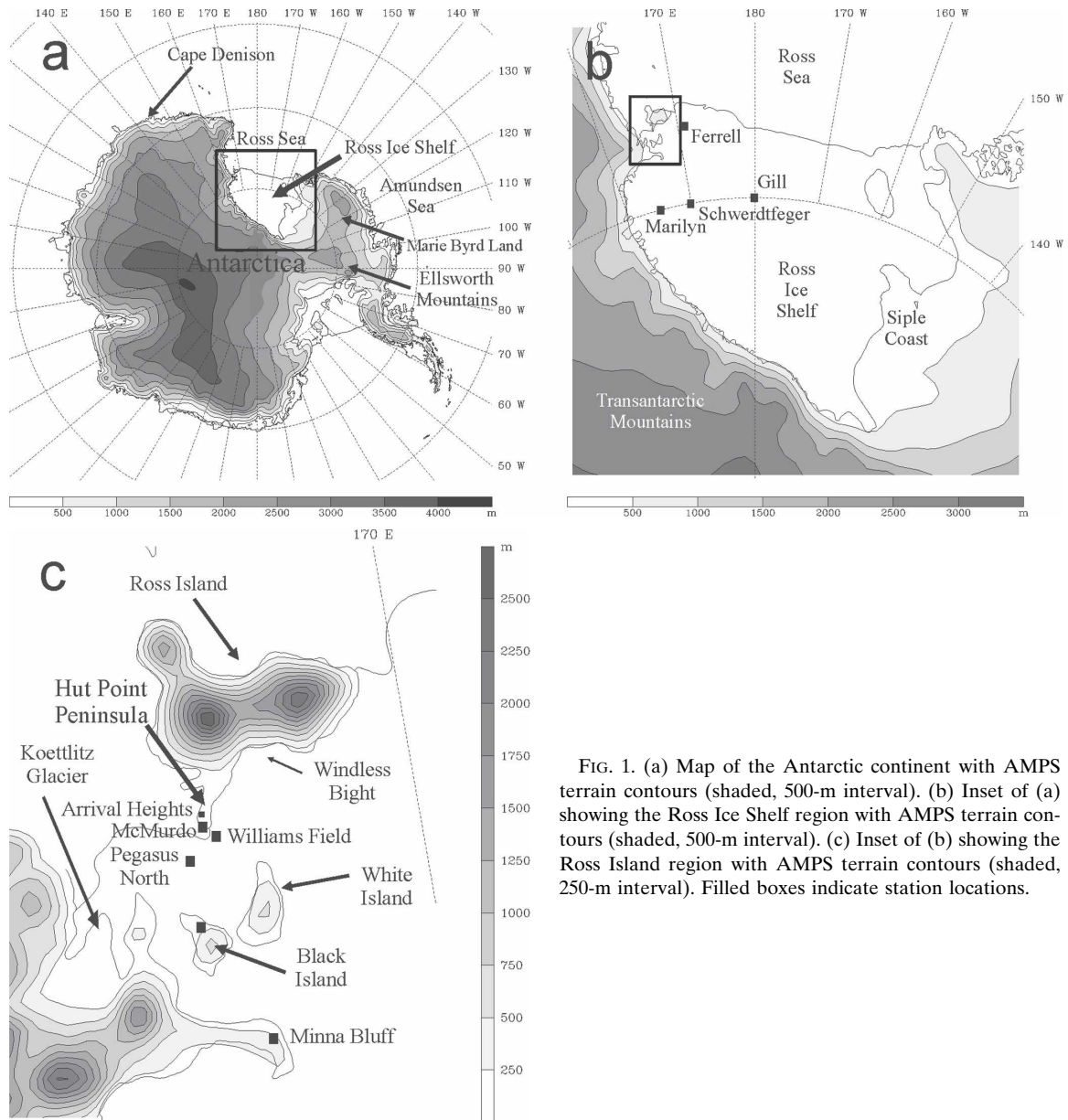


FIG. 1. (a) Map of the Antarctic continent with AMPS terrain contours (shaded, 500-m interval). (b) Inset of (a) showing the Ross Ice Shelf region with AMPS terrain contours (shaded, 500-m interval). (c) Inset of (b) showing the Ross Island region with AMPS terrain contours (shaded, 250-m interval). Filled boxes indicate station locations.

Accurate forecasting is critical for base operations at McMurdo. McMurdo is the logistical hub and the largest base of the U.S. Antarctic Program (USAP). During the main field season (October–February), McMurdo supports a population of over 1000 people; however, several hundred people remain at McMurdo during winter for operations and various research endeavors. Airstrips at McMurdo handle intercontinental flights to and from Christchurch, New Zealand, along with flights to and from the South Pole and other continental locations.

The primary goal of this paper is to analyze the atmospheric dynamics involved in producing the severe

winds at McMurdo. The minimum central pressure of a lower-tropospheric cyclone that tracks just east of McMurdo after 1800 UTC 15 May is increasing during the previous 12 h. Also, wind speed observations away from the McMurdo area (Ferrell, Gill, Schwerdtfeger, and Marilyn) never exceed 30 m s^{-1} . The dynamical processes involved in producing severe winds in the vicinity of a weakening cyclone, and in a localized area, are explored in this paper.

Forecast guidance for McMurdo and all of Antarctica is provided by the Antarctic Mesoscale Prediction System (AMPS; Powers et al. 2003), an experimental, real-time numerical weather prediction system developed

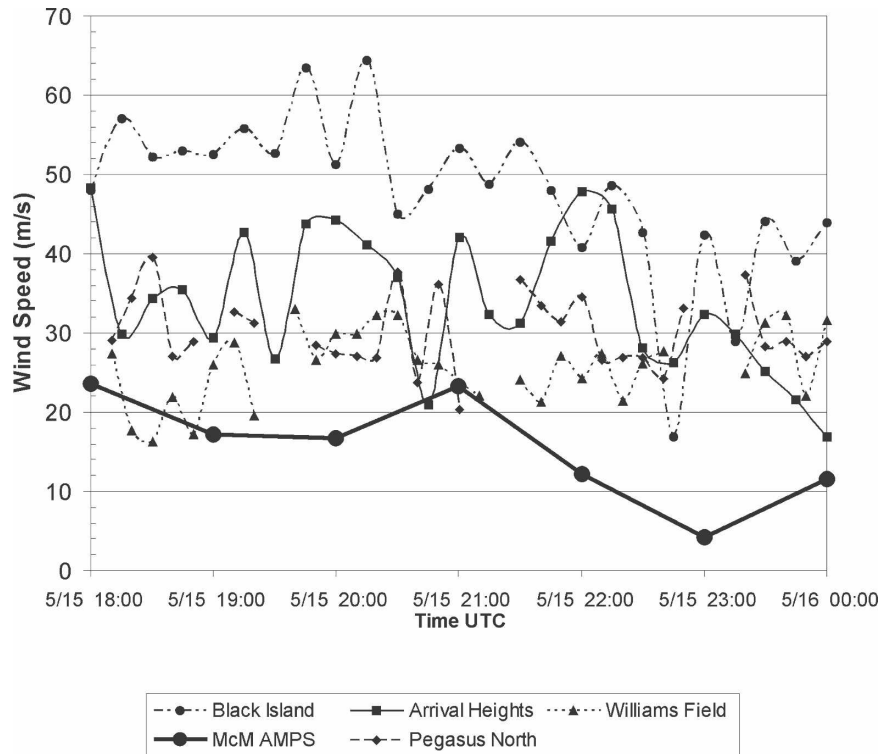


FIG. 2. Wind speed (m s^{-1}) at Black Island (dashed-dotted, small filled circles), Arrival Heights (solid line, filled squares), Williams Field (dotted line, filled triangles), Pegasus North (dashed line, filled diamonds), and McMurdo AMPS (heavy solid line, large filled circles) between 1800 UTC 15 May 2004 and 0000 UTC 16 May 2004.

for the USAP. A more detailed description of AMPS is provided in the next section. Another goal of this case study is to analyze errors in AMPS forecasts of wind speeds during the storm. Between 1800 UTC 15 May and 0000 UTC 16 May, the AMPS 3.3-km grid provides a credible forecast for most of the Ross Island region, except for the immediate McMurdo area, where the AMPS wind speed forecasts never exceed 25 m s^{-1} . Figure 2 shows McMurdo area wind speed observations and the 3.3-km AMPS wind speed forecast for McMurdo during the storm. At 2300 UTC 15 May, when observed wind speeds exceed 35 m s^{-1} at McMurdo (Dalrymple 2004) and 30 m s^{-1} in the surrounding region (Fig. 2), the AMPS forecasted wind speed at McMurdo is under 5 m s^{-1} . However, Fig. 3 shows that AMPS forecasts high wind speeds just 20 km upstream (south) of McMurdo at 2300 UTC. The reasons for these errors in wind speed magnitude and location are investigated.

The following section features a description of AMPS, along with information about automatic weather station (AWS) data and Moderate Resolution Imaging Spectroradiometer (MODIS) imagery used in this case study. A synoptic overview follows in section

3. Section 4 describes the characteristics and forcing of a barrier wind regime along the Transantarctic Mountains that is a precursor to the strong winds at McMurdo. Section 5 contains an analysis of hydraulic theory as an analog to the downslope windstorms that impact the McMurdo area, along with discussion of other mountain-wave theories and their application to this case. Errors in AMPS wind speed forecasts are analyzed in section 6, and in section 7 the study concludes with a general event analysis, and a discussion of the impact of recent improvements in AMPS in relation to this event and future research needs.

2. Model configuration and data

AMPS is a joint effort between the Mesoscale and Microscale Meteorology (MMM) Division of the National Center for Atmospheric Research (NCAR) and the Polar Meteorology Group of the Byrd Polar Research Center at The Ohio State University (OSU). AMPS employs the Polar fifth-generation Pennsylvania State University–NCAR Mesoscale Model (MM5; Grell et al. 1995), a version optimized for use in polar regions by OSU (Bromwich et al. 2001; Cassano et al.

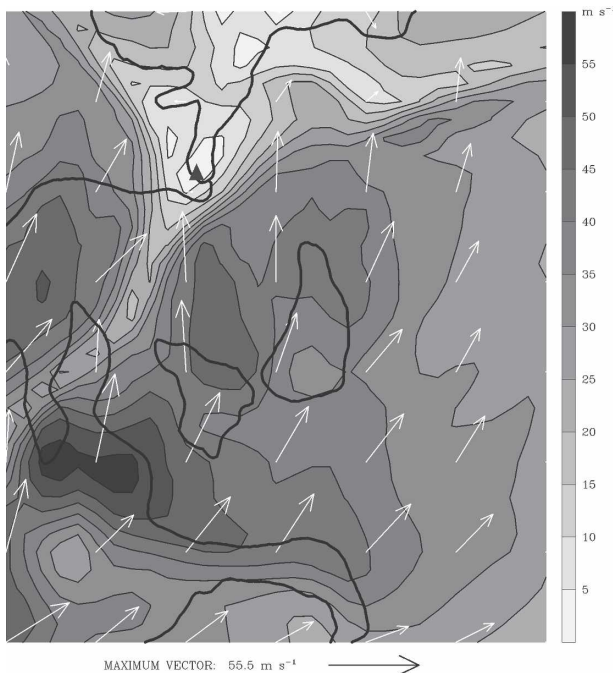


FIG. 3. Surface wind speed (m s^{-1}) and wind vectors (white arrows) from AMPS 3.3-km grid at 2300 UTC 15 May 2004. Contour and shade interval is 5 m s^{-1} . Black triangle indicates location of McMurdo.

2001). Polar MM5 includes a modified parameterization for the prediction of ice cloud fraction, improved cloud–radiation interactions, an optimal stable boundary layer treatment, improved calculation of heat transfer through snow and ice surfaces, and the addition of a fractional sea ice surface type (Bromwich et al. 2001).

The AMPS Polar MM5 consists of five polar stereographic domains. Domains 2 (30-km resolution), 3 (10-km resolution), and 5 (3.3-km resolution) are used in this analysis. There are 31 vertical half-sigma levels, with 11 levels in the lowest 1000 m to capture the complex interactions in the planetary boundary layer. The lowest half-sigma level is about 13 m above the surface. The model output is archived on the mass storage system (MSS) at NCAR.

The AMPS Polar MM5 is initialized twice daily at 0000 and 1200 UTC. The initial and boundary conditions are derived from the National Centers for Environmental Prediction Global Forecasting System (GFS) model. The GFS first-guess field is objectively reanalyzed with the available observations using a multiquadric technique (Nuss and Titley 1994). The observations available for assimilation into AMPS include reports from radiosondes, Synoptic Surface Observation (SYNOP) reports, AWS observations, ship reports, and buoys. Satellite-derived cloud-track winds

are also assimilated in the 90-km grid. AMPS ingests sea ice data daily from the National Snow and Ice Data Center for its fractional sea ice depiction.

Guo et al. (2003) evaluate Polar MM5 performance over Antarctica for a 1-yr period (1993) on a 60-km resolution domain and show that the intra- and interseasonal variability in pressure, temperature, wind, and moisture are well resolved. Bromwich et al. (2005) evaluate 2-yr of AMPS Polar MM5 forecasts on the 30-km domain and show that the same variables are well resolved at synoptic time scales as well. Therefore, we consider the quality of the model forecasts to be suitable for use in this study.

For AMPS 30- and 10-km grids, 12–21-h forecasts are used at 3-h intervals. For example, between 1200 and 2100 UTC 15 May, forecasts from the 0000 UTC 15 May model run are used. For the 3.3-km grid, forecasts are at 1-h intervals, with the 0000 UTC 15 May model run used prior to 2100 UTC 15 May and the 1200 UTC 15 May model run used from 2100 UTC 15 May onward. This is done because forecasts from the 1200 UTC 15 May model run provide more realistic representations of actual conditions than forecasts from the 0000 UTC 15 May model run during the most crucial time period of the case study. Forecasts from 12 h onward are used to allow sufficient time for the spinup of model fields. All AMPS forecasts for specific station locations use the 3.3-km grid. For all figures, the 30-km grid is used unless otherwise indicated, and representations of surface variables are done at the lowest half-sigma level.

Surface observations are obtained from the Antarctic Meteorological Research Center (AMRC) at the University of Wisconsin—Madison (UW; <http://amrc.ssec.wisc.edu>). Data from UW-AWS sites and Space and Naval Warfare Systems Center (SPAWAR)-AWS sites are archived at AMRC and are used in this case study. Station pressure values are adjusted to mean sea level to facilitate analysis. Temperature, wind speed, and wind direction observations at a height of 3 m are also used in analysis. UW-AWS observations are instantaneous at a 10-min frequency; SPAWAR AWS observations are averages of 2-min observations at a 15-min frequency. Further information regarding UW automatic weather stations can be found in Stearns et al. (1993). MODIS imagery from the *Terra* and *Aqua* satellites of the Earth Observing System (EOS) at 5- and 1-km resolution is obtained from the Goddard Earth Science (GES) Distributed Active Archive Center (DAAC; <http://daac.gsfc.nasa.gov>). Raw data images are combined and remapped using Man computer Interactive Data Access System (McIDAS) software.

MODIS band 31, at a wavelength of approximately $11.03 \mu\text{m}$, is used for this case study. MODIS imagery is used primarily for cyclone tracking throughout the case study.

3. Synoptic overview

a. Cyclone track

According to AMPS (AWS coverage is insufficient and a satellite gap prevents use of MODIS imagery) the cyclone of interest for this case study moves onto Marie Byrd Land from the Amundsen Sea after 1200 UTC 14 May and descends onto the Ross Ice Shelf near the Siple Coast after 0300 UTC 15 May. Figure 4 shows a track comparison of the cyclone between AMPS and AWS/MODIS, along with the minimum sea level pressure of the cyclone in AMPS. From 0600 UTC 15 May until 0000 UTC 16 May, the minimum central pressure of the cyclone increases by 45 hPa in AMPS, which is an average rate of 2.5 hPa h^{-1} for the 18 h. Analysis of AWS sea level adjusted pressure values show general agreement with AMPS in regards to pressure tendencies through 2100 UTC 15 May, with AWS values having similar tendencies, but being 1–4 hPa lower than AMPS during this time. AMPS places the cyclone farther south and several hours ahead (about 3 h at 0600 UTC to under an hour by 1800 UTC) of the observed cyclone throughout the case study. It is unclear if the track difference has any effect on cyclone strength, or if the AMPS bias can be attributed to analysis error.

b. 500-hPa analysis

Figures 5a–c show the 500-hPa geopotential height distribution and horizontal advection of absolute vorticity at 6-h intervals between 0600 and 1800 UTC 15 May. At 0600 UTC (Fig. 5a) the surface cyclone is collocated with a region of weak anticyclonic vorticity advection aloft, implying downward vertical motion. At 1200 UTC (Fig. 5b) the cyclone is collocated with a region of weak cyclonic vorticity advection, meaning that upward vertical motion should be supporting cyclone intensification. At 1800 UTC (Fig. 5c) there is negligible vorticity advection in the vicinity of the cyclone. Figures 5a–c show that vorticity advection at 500 hPa is dominated by weak and transient short waves located between two deeper troughs that are associated with the geopotential minimum to the north over the Ross Sea and that upper-level forcing is weak overall. To determine the robustness of vorticity advection with the presence of topography upstream, potential vorticity (PV) advection on the 288-K isentropic level in AMPS was plotted (not shown), and the advection pat-

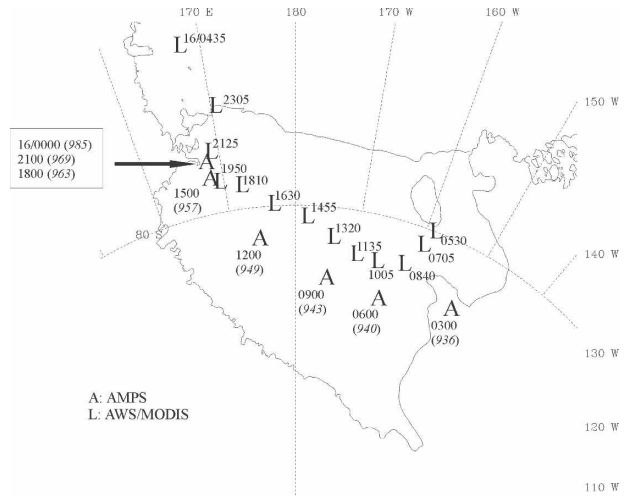


FIG. 4. Cyclone track for AMPS (A) and observed (AWS/MODIS, L). Italicized numbers in parentheses indicate minimum sea level pressure of cyclone. Times are in UTC for 15 May 2004 unless otherwise indicated.

terns are similar to those on the 500-hPa vorticity advection plot.

c. Low-level analysis

At the surface, a large potential temperature contrast is present between the warm air over West Antarctica (east of the cyclone) and the cold air over the north-central Ross Ice Shelf (west of the cyclone) at 0000 UTC 15 May (Fig. 6a). The latter appears to form due to radiational cooling over the previous 12 h. The thermal contrast is strongest at the surface, as the region of cold air over the Ross Ice Shelf is shallow and restricted to the layer beneath 850 hPa. At 0600 UTC (Fig. 6b), the cold air is wrapping around the eastern side of the cyclone, while the source of warm air southeast of the cyclone is being cut off by the Transantarctic Mountains and the Ellsworth Mountains over the continental interior. At 1200 UTC (Fig. 6c), the warm air has been cut off, and the potential temperature distribution resembles an occlusion, with cold air wrapping around the entire cyclone. Warm air over the Transantarctic Mountains persists but does not interact with cold air at lower elevations over the Ross Ice Shelf. By 1800 UTC (Fig. 6d) the thermal contrast around the cyclone has weakened compared with previous analysis times. The weakening of the thermal gradient around the cyclone in Figs. 6a–d is the primary cause of the rises in minimum central pressure of the cyclone. Fundamental to the development and maintenance of cyclones is production of a low-level thermal ridge downstream of the cyclone, which is achieved through lower-tropospheric

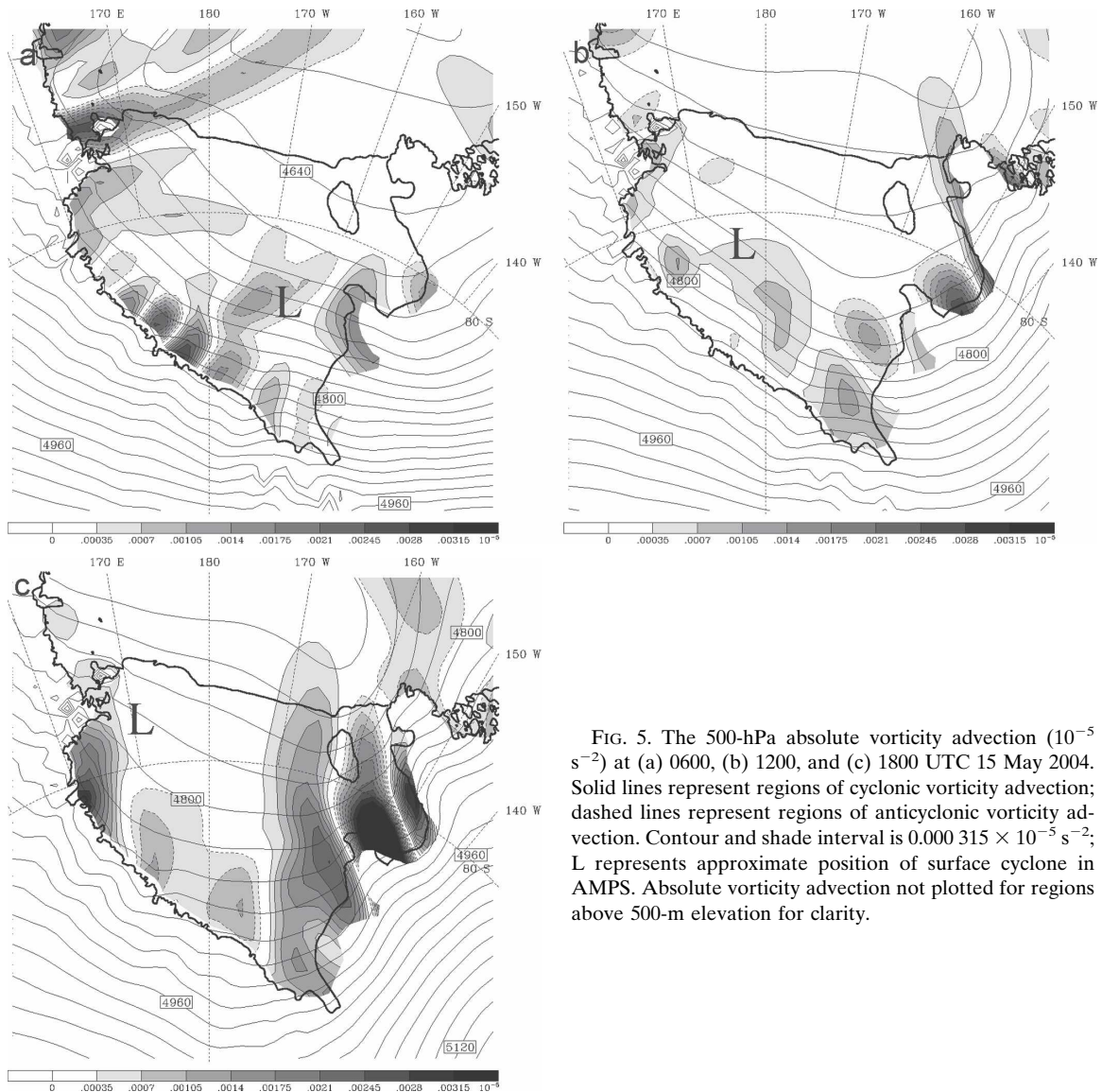


FIG. 5. The 500-hPa absolute vorticity advection (10^{-5} s^{-2}) at (a) 0600, (b) 1200, and (c) 1800 UTC 15 May 2004. Solid lines represent regions of cyclonic vorticity advection; dashed lines represent regions of anticyclonic vorticity advection. Contour and shade interval is $0.000315 \times 10^{-5} \text{ s}^{-2}$; L represents approximate position of surface cyclone in AMPS. Absolute vorticity advection not plotted for regions above 500-m elevation for clarity.

warm air advection. Figure 7a shows that at 0600 UTC, there is a broad region of warm air advection downstream (northwest) of the cyclone and a region of cold air advection upstream (southeast) of the cyclone, implying a favorable setup at the surface for cyclone development. Potential temperature advection at 1200 UTC (Fig. 7b) shows that the region of warm air advection downstream of the cyclone has shrunk and weakened in the past 6 h because of the blocking of the warm air source region by the Transantarctic and Ellsworth Mountains. Two regions of cold air advection are present, centered just east of the international date line. The southernmost region of cold air advection is rotating around the cyclone and is located downstream of the cyclone by 1800 UTC (Fig. 7c). A region of warm

air advection is located upstream of the cyclone, so that in the 12 h between 0600 and 1800 UTC the low-level thermal advection pattern completely reverses orientation. To determine the vertical structure above the region of surface cold air advection, a cross section is taken along the flow and through the aforementioned cold air advection region at 1200 UTC, indicated in Fig. 7b and shown in Fig. 8. Cold air advection at the surface, coupled with a thermal maximum at about 850 hPa, results in a stable lower-tropospheric environment that hinders upward vertical motions. The cessation of warm air advection downstream of the cyclone, combined with the lack of upper-tropospheric support, is the likely cause of cyclolysis after 0600 UTC.

Given the large increase in minimum surface pres-

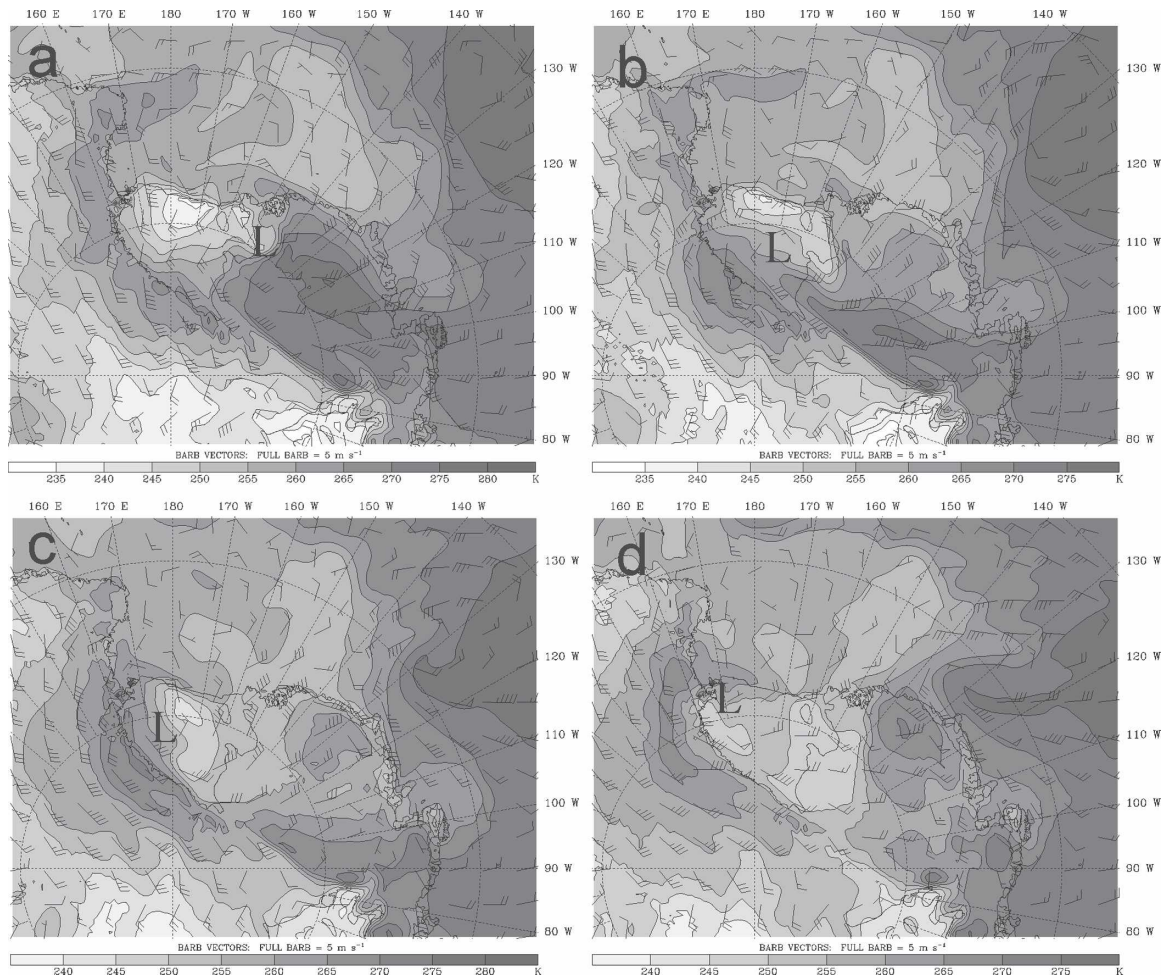


FIG. 6. Surface potential temperature (contoured and shaded, interval 5 K) and wind barbs (full barb = 5 m s⁻¹) at (a) 0000, (b) 0600, (c) 1200, and (d) 1800 UTC 15 May 2004; L represents approximate position of surface cyclone in AMPS.

sure of the cyclone during the case study period, the isallobaric wind is analyzed to assess the influence of the pressure change field on large-scale forcing. The isallobaric wind,

$$\mathbf{V}_{\text{isal}} = -\frac{1}{f^2} \nabla \frac{\partial \Phi}{\partial t}, \quad (1)$$

is the component of the ageostrophic wind that is proportional to the gradient of geopotential tendency (on a constant pressure surface), directed toward regions of maximum height falls. Figure 9 shows the simulated actual wind at 0900 UTC and the isallobaric wind computed with the time tendency between 0900 and 1200 UTC over the Ross Ice Shelf at 925 hPa in AMPS. In the southwestern quadrant of the cyclone, the isallobaric wind has a similar orientation to the actual wind, as expected with northwestward propagation of the cyclone. The gradients of the pressure change field are a

key component of the large-scale forcing in the southwestern quadrant of the cyclone. The isallobaric wind has decreasing influence with proximity to the Transantarctic Mountains, implying that topographic effects provide additional forcing for strong winds in this region.

4. Barrier wind

a. Identification

Northwestward propagation of the cyclone across the Ross Ice Shelf between 0900 and 1800 UTC 15 May is shown at 3-h intervals in Figs. 10a–d. Wind speeds in the western sector of the cyclone along the base of the Transantarctic Mountains exceed 30 m s⁻¹, higher than wind speeds in the eastern sector of the cyclone, which never exceed 20 m s⁻¹ after 0900 UTC (Figs. 10a–c). By 1800 UTC (Fig. 10d), a core of wind speeds greater than

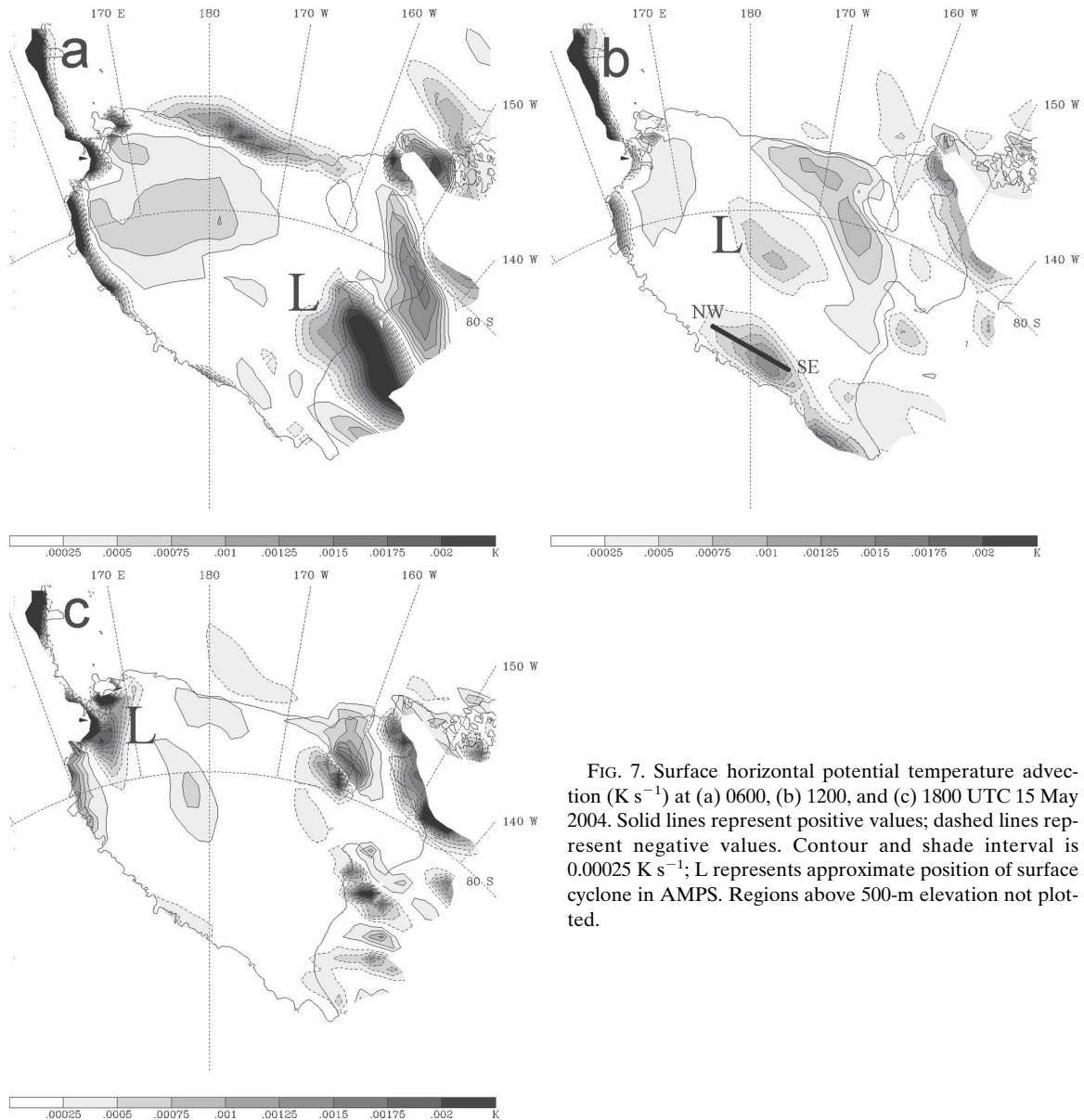


FIG. 7. Surface horizontal potential temperature advection (K s^{-1}) at (a) 0600, (b) 1200, and (c) 1800 UTC 15 May 2004. Solid lines represent positive values; dashed lines represent negative values. Contour and shade interval is 0.00025 K s^{-1} ; L represents approximate position of surface cyclone in AMPS. Regions above 500-m elevation not plotted.

25 m s^{-1} remains in the western sector of the cyclone. AMPS places the cyclone east of Minna Bluff, and the surface pressure field associated with the cyclone has become deformed into an oval shape, while in the western sector of the cyclone the surface pressure gradient has intensified compared with the previous 9 h. To determine the magnitude of the pressure gradient intensification, measurements of the AMPS pressure gradient on the western and eastern sides of the cyclone are taken along the transect indicated on each map in Fig. 10 and displayed in Table 1. The pressure gradient is of similar magnitude along both the eastern and western sides of the cyclone until 1500 UTC. By 1800 UTC, the pressure gradient along the western edge is increasing,

while the gradient along the eastern edge is remaining nearly steady. The observed pressure difference between Marilyn AWS and Schwerdtfeger AWS is shown in Fig. 11. The Marilyn–Schwerdtfeger pressure gradient cannot be directly compared with AMPS because of the difference in cyclone track between AMPS and reality. However, the trends of the AMPS pressure gradient west of the cyclone and the Marilyn–Schwerdtfeger pressure gradient can be compared to gauge the validity of the pressure gradient intensification west of the cyclone in the model. The Marilyn–Schwerdtfeger pressure difference shows a similar trend to the model difference, with a relatively steady pressure difference until about 1500 UTC, after which

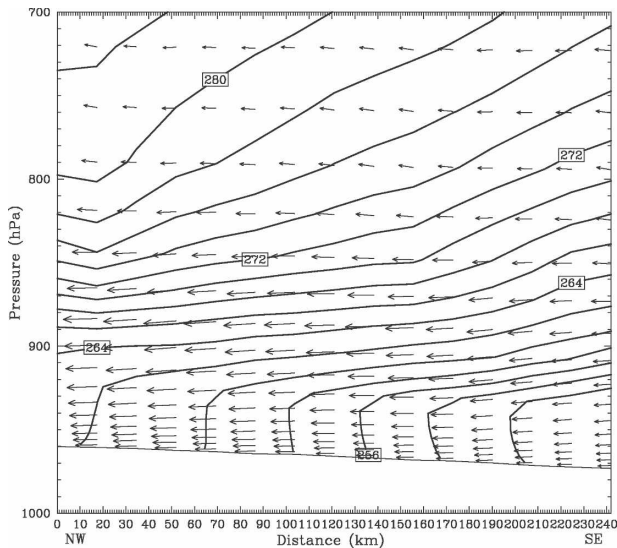


FIG. 8. Cross section of potential temperature (2-K contour interval) and along cross-section wind vectors (arrows) along transect indicated in Fig. 7b.

it increases. At 2100 UTC (not shown) the pressure gradient along the western edge is 3 times the size of the gradient along the eastern edge for both the 30- and 10-km grid forecasts in AMPS.

The intensification of the pressure gradient and resulting core of strong winds in the western sector of the cyclone are caused by a barrier wind. As the cyclone moves onto the Ross Ice Shelf, northerly flow in the southeastern quadrant of the cyclone impinges upon the Transantarctic Mountains at the southern tip of the Ross Ice Shelf by 0900 UTC (Fig. 10a). Flow directed orthogonal to the Transantarctic Mountains will either have sufficient momentum to flow over the topography or will be forced around. The resulting flow regime will depend upon the wind speed, the height of the barrier, and the stability of the layer in front of the barrier (O'Connor et al. 1994). Whether the flow will traverse the topography or be deflected around can be determined from the Froude number:

$$Fr = U_0 \left(gH \frac{\Delta\theta}{\theta} \right)^{-1/2}, \quad (2)$$

where U_0 is the wind speed, g is the gravitational acceleration (9.8 m s^{-2}), H is the height of the obstacle, $\Delta\theta$ is the increase in potential temperature between the surface and the top of the obstacle, and θ is the average potential temperature of the layer between the surface and the height of the obstacle. If $Fr \geq 1$, the flow will have sufficient kinetic energy to traverse the topography, whereas $Fr < 1$ indicates a lack of kinetic energy to traverse the topography, and flow will be forced

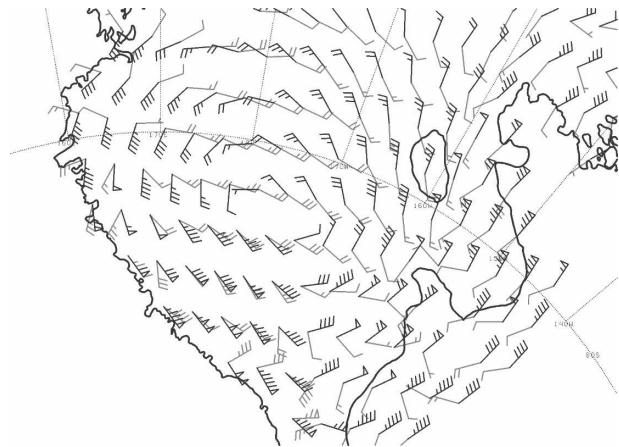


FIG. 9. Actual (black) and isobaric (gray) wind barbs (full barb = 5 m s^{-1}) at 925 hPa. Actual wind is at 0900 UTC 15 May; isobaric wind computed from pressure change tendency between 0900 and 1200 UTC 15 May.

around. Using representative values from the AMPS forecast for the Transantarctic Mountains at the southern end of the Ross Ice Shelf at 0900 UTC 15 May, $U_0 = 17.5 \text{ m s}^{-1}$, $H = 2000 \text{ m}$, $\Delta\theta = 16 \text{ K}$, $\theta = 270 \text{ K}$, and $Fr \approx 0.51$. Since $Fr < 1$, the flow will not have sufficient kinetic energy to traverse the Transantarctic Mountains. Typically, a layer of cold air at the base of the mountain deepens, causing the pressure gradient to strengthen. However, in this case, air at the surface is warmer at the base of the mountain compared with conditions upwind (to the north), as indicated in Fig. 10a, due to cold air advection from the north. Even without the cold pool at the base of the mountains, the stratification and terrain height are sufficient to cause blocking. A mesoscale pressure gradient develops, directed perpendicular to and away from the mountains. A force balance is created between the pressure gradient force and the Coriolis force (directed to the left in the Southern Hemisphere). The result is a barrier wind that flows with the barrier to the left side (southerly for this case).

Identification of a barrier wind along the Transantarctic Mountains is obscured by storm motion. From 0600 until 1800 UTC 15 May the cyclone moves rapidly northwestward, nearly parallel to the Transantarctic Mountains. Removal of storm motion allows for clearer identification of barrier wind effects. Storm-relative wind vectors are plotted over the sea level isobars in Figs. 12a–d. At 0900 UTC (Fig. 12a), storm-relative winds between the cyclone and the Transantarctic Mountains are southerly to southeasterly and down-slope off of the Transantarctic Mountains. At 1200 UTC (Fig. 12b) flow along the base of the Transantarctic Mountains is transitioning from south-southeasterly to

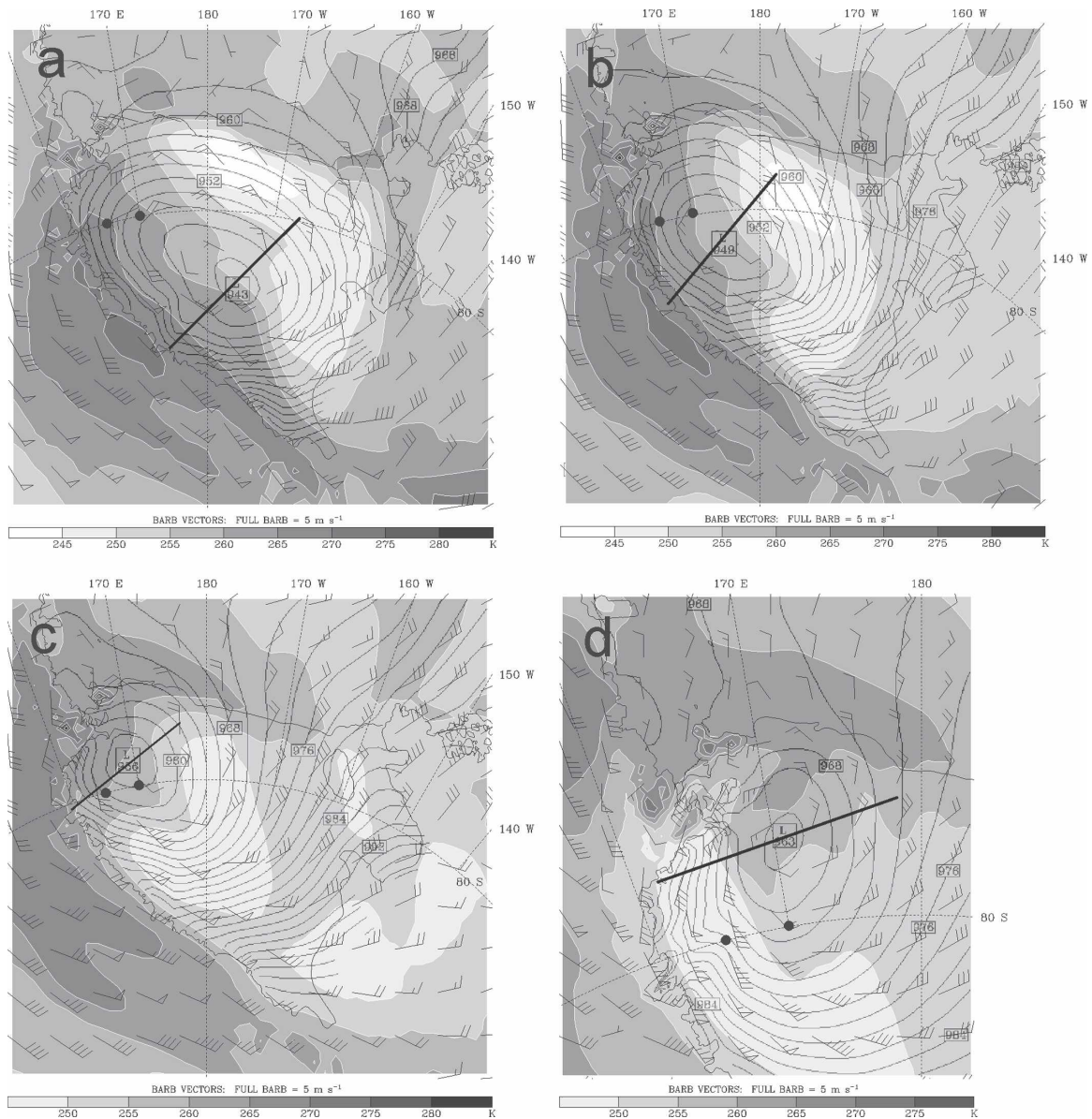


FIG. 10. Sea level pressure (contoured, 2-hPa contour interval), surface potential temperature (shaded, interval 5 K), and surface wind barbs (full barb = 5 m s^{-1}) from AMPS 30-km grid at (a) 0900, (b) 1200, and (c) 1500 UTC 15 May 2004, and (d) from the AMPS 10-km grid at 1800 UTC 15 May 2004. Thick black line represents transect used for pressure gradient magnitude calculation in Table 1. Black dots represent locations of Schwerdtfeger and Marilyn AWS sites.

a southeasterly flow, indicating the initiation of barrier wind forcing. By 1500 UTC (Fig. 12c), southeasterly storm-relative wind speeds greater than 20 m s^{-1} north-west of 180° along the Transantarctic Mountains indicate that downslope wind forcing has been shut off by the synoptic pressure gradient associated with the cyclone and has been replaced by the barrier wind. The 1800 UTC analysis (Fig. 12d) shows the barrier wind extending north of 80°S . Storm motion has slowed considerably, while storm-relative wind speeds in the west-

ern sector of the cyclone increase and become stronger than wind speeds in the eastern sector of the cyclone. The approximate 6-h lag period between barrier-perpendicular pressure gradient forcing (0900 UTC) and barrier wind response (1500 UTC) is justified for a synoptic-scale barrier wind event (O'Connor et al. 1994).

Another possible explanation for the core of high wind speeds along the western edge of the cyclone is an increase in the synoptic pressure gradient to the west.

TABLE 1. Sea level pressure difference [hPa (100 km)⁻¹] for the west and east sides of the cyclone from AMPS 30-km grid between 0900 and 1500 UTC 15 May 2004 and AMPS 10-km grid at 1800 UTC 15 May 2004. Distance refers to transect specified in Fig. 10 at corresponding time for pressure gradient calculation.

Time (UTC)	Distance (km)	West [hPa (100 km) ⁻¹]	East [hPa (100 km) ⁻¹]
0900	240	5	5
1200	175	6	4
1500	140	6	4
1800	190	10.5	4.5

The 500-hPa geopotential height field can be used over the high-altitude regions west of the Ross Ice Shelf to determine near-surface effects, as sea level pressure adjustment is unreliable there. A moderate geopotential height gradient does exist south of the Ross Ice Shelf and over East Antarctica, although the gradient does not increase in magnitude between 0600 (Fig. 13a) and 1800 UTC (Fig. 13b), it actually weakens, implying that the synoptic pressure gradient is not causing the increase in the pressure gradient in the western sector of the cyclone between 1500 and 2100 UTC. However, Fig. 13a illustrates the influence of the large-scale geopotential height gradient on the formation of the barrier wind. The strong gradient in geopotential height southeast of the Ross Ice Shelf in Fig. 13a originates from a ridge over the Weddell Sea (not shown). The near-surface ridge of geopotential height over the continental interior and the presence of the cyclone over the central Ross Ice Shelf cause a strong surface pressure gradient to form over the southeastern Ross Ice Shelf, as shown in Figs. 10a and 10b. This pressure gradient results in wind speeds of 20 m s⁻¹ to impinge upon the Transantarctic Mountains through 1200 UTC 15 May.

b. Momentum forcing

Despite the clear presence of a barrier wind along the Transantarctic Mountains, the momentum forcing within the region between the cyclone and the Transantarctic Mountains is also influenced by the evolving horizontal pressure gradient (due to the interactions between mass accumulation and the synoptic-scale pressure gradient associated with the cyclone) and accelerations (due to flow curvature and momentum advection). An analysis of the terms in the equations of motion is done to better understand the physical forcing associated with the strong winds in the barrier wind region. Terms from the model-based x - and y -component equations of motion are computed on the 925-hPa isobaric surface. The 925-hPa isobaric surface

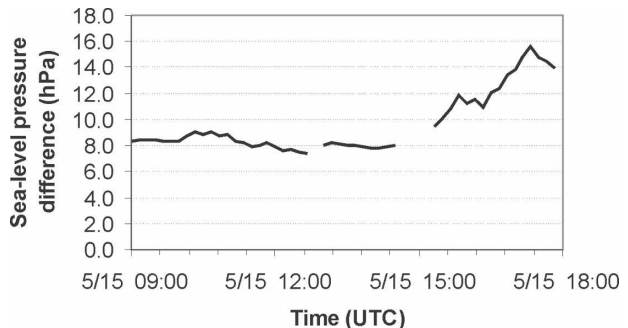


FIG. 11. Sea level pressure (hPa) difference between Marilyn AWS and Schwerdtfeger AWS between 0900 and 1800 UTC 15 May 2004.

is used so that the effects of friction are reduced, while barrier wind effects can still be represented and the analysis remains above the surface in the region of interest. The analysis is done on a constant pressure surface rather than a sigma surface to facilitate interpretation, as terms in the isobaric equations of motion are more familiar than those in the sigma coordinate equations. Since the analysis is taken over a relatively flat surface, isobars will be approximately parallel to model sigma levels in the vertical, so that significant differences would not be expected between coordinate systems. Variables are interpolated to 925 hPa from the two bounding sigma surfaces. A logarithmic interpolation routine is used for geopotential height and a linear interpolation routine is used for the other variables. The x - y coordinate system is rotated so that the equation of motion in the along-flow (y) direction is

$$-m \frac{\partial \Phi}{\partial y} - fu - \frac{\partial v}{\partial t} - \mathbf{V} \cdot \nabla \mathbf{v} = R_y, \quad (3)$$

and the equation of motion in the cross-flow (x) direction is

$$-m \frac{\partial \Phi}{\partial x} + fv - \frac{\partial u}{\partial t} - \mathbf{V} \cdot \nabla \mathbf{u} = R_x, \quad (4)$$

where

$$\mathbf{V} \cdot \nabla \mathbf{A} = mu \frac{\partial A}{\partial x} + mv \frac{\partial A}{\partial y} + \omega \frac{\partial A}{\partial p}, \quad (5)$$

m is a map factor based on the polar stereographic projection used in the model, R_x and R_y are the residual terms (which include friction), and the rest of the terms have their usual meteorological meaning. From a scale analysis of both horizontal momentum equations, curvature terms and the vertical components of the Coriolis force are neglected. Horizontal partial derivatives are estimated using a fourth-order centered-difference

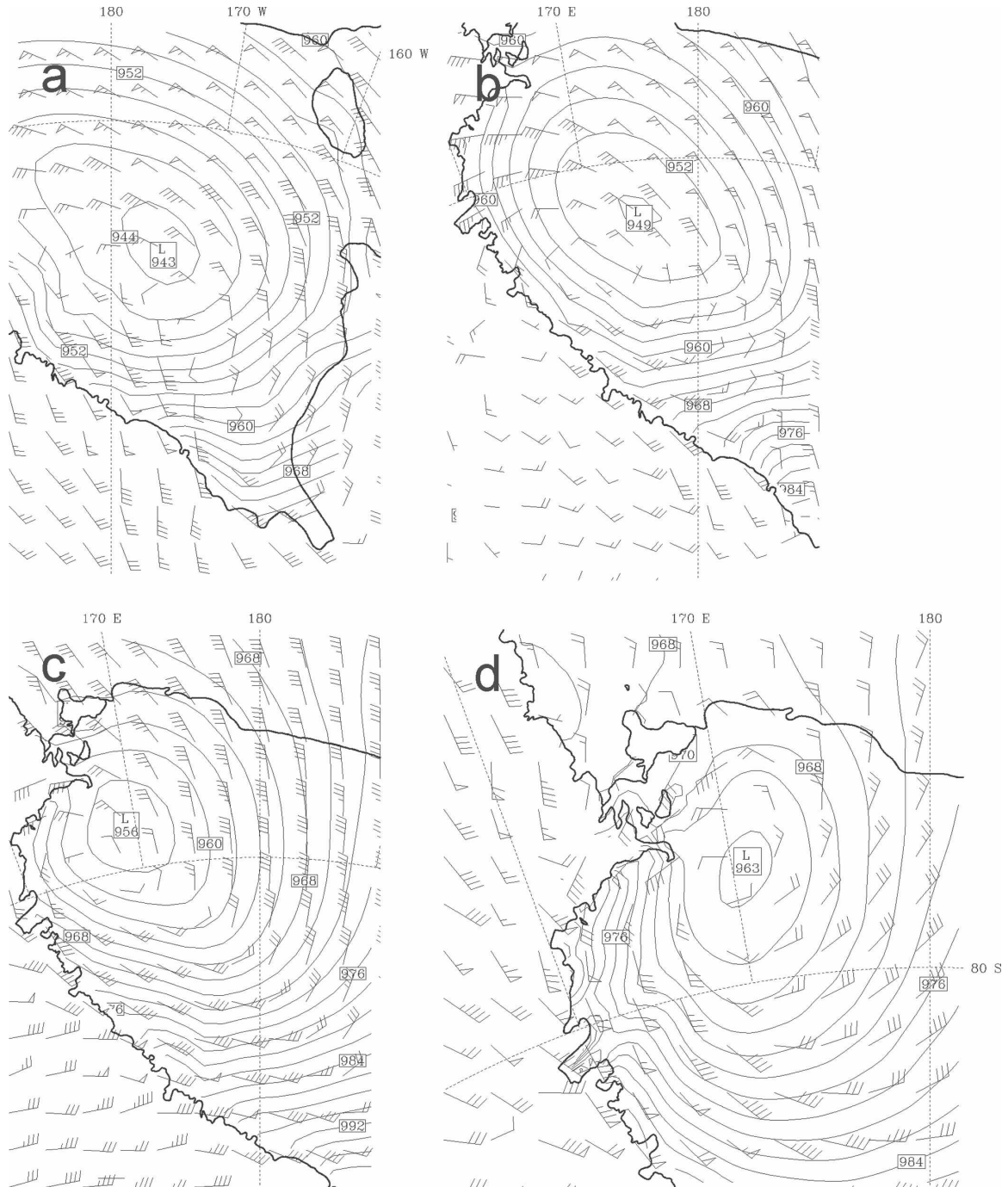


FIG. 12. Sea level pressure (hPa) and surface storm-relative winds (relative to a path of storm motion 3 h before to 3 h after, and magnitude of 17.1 m s^{-1}) at (a) 0900 UTC 15 May 2004. (b) Storm motion of 19.2 m s^{-1} at 1200 UTC 15 May 2004. (c) Storm motion of 12 m s^{-1} at 1500 UTC 15 May 2004. (d) Storm motion of 2.9 m s^{-1} at 1800 UTC 15 May 2004 using AMPS 10-km grid. Contour interval is 2 hPa and full barb = 5 m s^{-1} .

scheme, described in Haltiner and Williams (1980, chapter 5); partial derivatives in time are estimated with a time step of 1 h; and partial derivatives in the vertical are estimated over a 30-hPa vertical layer, centered on 925 hPa.

Terms are grouped together as follows: the first term in (3) and (4) is the height gradient force term (HGF). The next term is the Coriolis force term (COR), which is zero by definition in the along-flow direction (except for the neglected vertical component). The next term in

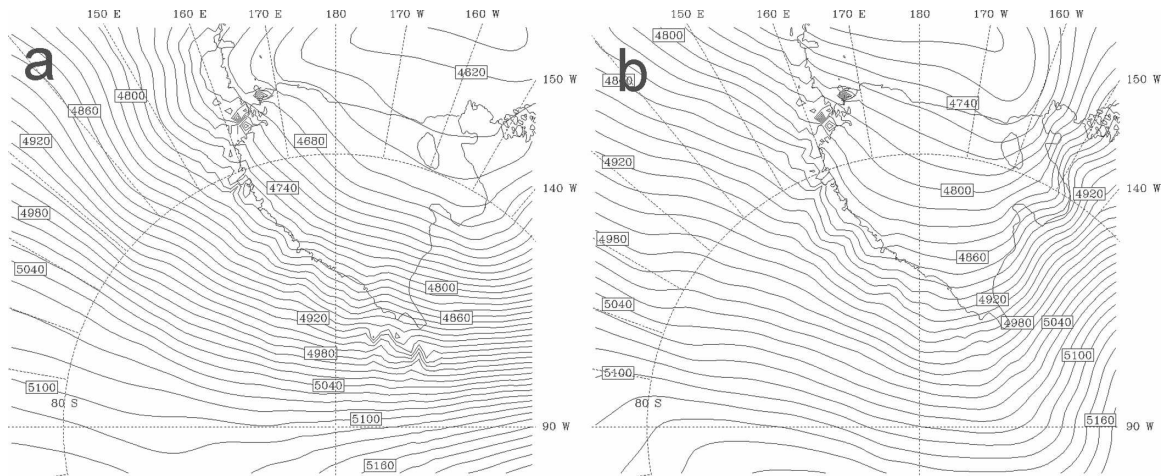


FIG. 13. The 500-hPa geopotential height (m) at (a) 0600 and (b) 1800 UTC 15 May 2004. Contour interval is 15 m.

each equation is the local time tendency of the velocity (LC). The following term represents the advection of momentum, expanded in (5), and grouped as (ADV). The residual is a combination of friction and error. With along- and cross-flow components at each grid point, values are averaged in four 5×5 grid boxes to obtain a more robust result for the region of interest. Two averaging boxes (A and B) are computed at 1500 UTC and shown in Fig. 14a, and two (C and D) are computed at 1800 UTC and shown in Fig. 14b. The locations for each box were chosen in an attempt to limit spurious effects from the terrain to the west while remaining within the barrier jet. Results of the computations for each box are shown in Table 2. Box A has

been chosen to represent the developing barrier wind regime at 1500 UTC, where flow is accelerating down the height gradient in the along-flow direction, while in the cross-flow direction there is nearly geostrophic balance, with ADV countering the excess HGF. Box B represents flow at the leading edge of the barrier wind. The along-flow ADV term is larger than in box A, and an approximate balance is forged between LC (due to changes in flow direction with time) and ADV (positive momentum advection), indicating that upstream barrier wind effects are beginning to impact this region. There is approximate geostrophic balance in the cross-flow direction. Box C is in the same location as box B and is chosen to represent the developing barrier wind

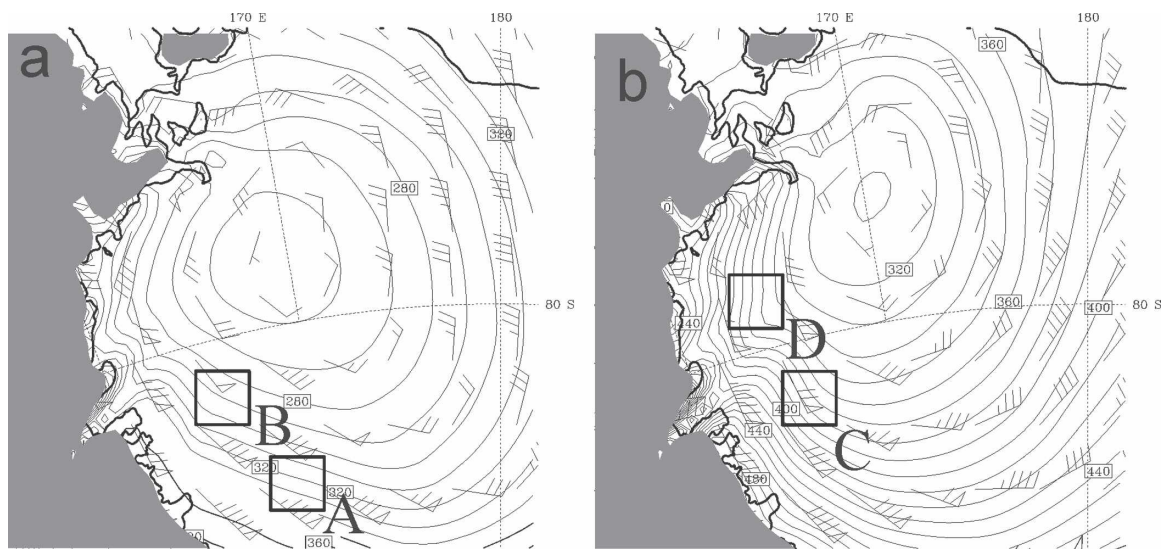


FIG. 14. The 925-hPa geopotential height (m) and wind barbs at (a) 1500 and (b) 1800 UTC 15 May 2004. Contour interval is 10 m. Full barb = 5 m s^{-1} . Boxes described in text.

TABLE 2. Magnitude of components ($\times 10^{-4} \text{ m s}^{-2}$) of horizontal momentum equation at 925 hPa. Location corresponds to averaging box in Figs. 14a and 14b. Cross-flow components are positive to right of flow.

Time (UTC)	Box	Along					Cross				
		HGF	COR	LC	ADV	RES	HGF	COR	LC	ADV	RES
1500	A	20	0	-24	8	4	64	-58	3	-18	-9
1500	B	13	0	-38	32	6	45	-46	6	-13	-8
1800	C	3	0	19	3	25	77	-49	9	-52	-15
1800	D	-21	0	-3	40	16	75	-51	<1	-27	-3

at 1800 UTC. Forcing in the along-flow direction is weaker compared with box B; however, the cross-flow HGF is larger and an approximate geostrophic balance is no longer valid. The increase in HGF is due to the continued mass accumulation against the Transantarctic Mountains, forced by flow into the barrier in the southern sector of the cyclone. HGF is countered by both COR and ADV, where the latter has increased in magnitude since 1500 UTC from negative momentum advection due to the effects of cyclonic curvature to the east. In a typical barrier wind event, an approximate geostrophic balance develops between the mesoscale pressure gradient force and the Coriolis force. The cyclonic curvature in this region will cause flow to be subgeostrophic. The increase in magnitude of $\partial u/\partial x$ and $\partial u/\partial y$ in the cross-flow advection term, due to the combined effects of cyclonic curvature and the barrier wind, causes a further departure from geostrophic balance. The large residual values for this box are attributed to errors in finite differencing due to the large degree of flow curvature. Box D features an along-flow balance between the retarding HGF and positive ADV terms, and the cross-flow balance is similar to box C except that ADV is smaller. Overall, the barrier wind system develops substantially between 1500 and 1800 UTC, evidenced by the increase in cross-flow HGF. Contrary to typical barrier wind events, an approximate geostrophic balance is not valid for the regions described at 1800 UTC, as negative momentum advection due to flow curvature forces a three-way balance in the cross-flow direction between the height gradient force, Coriolis force, and momentum advection.

c. Effects of barrier wind at McMurdo

Wind speeds of 25–35 m s^{-1} associated with the barrier wind are not directly responsible for the intense windstorm at McMurdo. However, the barrier wind is an important component to the McMurdo windstorm. The intensification of the pressure gradient between 80°S and Minna Bluff allows for strong wind speeds to persist past the region of barrier wind formation. Without the barrier wind intensification of the synoptic pres-

sure gradient, wind speeds approaching Minna Bluff would decrease as the flow adjusts to the weaker pressure gradient associated with the cyclone. Furthermore, without the barrier wind forcing, wind speeds in the western sector of the dissipating cyclone would be similar to those found in the eastern sector, between 10 and 15 m s^{-1} at 1800 UTC. Froude number calculations for Minna Bluff from AMPS at 1800 UTC using $U_0 = 12.5 \text{ m s}^{-1}$, $H = 1000 \text{ m}$, $\Delta\theta = 4 \text{ K}$, and $\theta = 256 \text{ K}$ give $Fr \approx 1.01$. Minna Bluff and Black Island would both cause blocking effects for wind speeds under 12.5 m s^{-1} . As will be shown in the next section, continual overriding of Minna Bluff and Black Island due to strong barrier winds and a Froude number greater than one are important for development of the windstorm at McMurdo. Last, the barrier wind enhances low-level cold air advection. Figure 10 shows that cold potential temperature air at the surface over the north-central Ross Ice Shelf at 0900 UTC (Fig. 10a) is entrained into the cyclonic circulation and approaches Minna Bluff by 1800 UTC (Fig. 10d). Without the barrier wind, the core of cold air would not reach the region by 1800 UTC. The cold air near the surface increases low-level stability and is shown to be an important feature of downslope windstorms in the next section.

5. Downslope windstorms

a. Hydraulic theory

AMPS indicates that southerly barrier winds have sufficient kinetic energy to traverse both Minna Bluff and Black Island after 1800 UTC 15 May, as $U_0 = 20 \text{ m s}^{-1}$, $H = 1000 \text{ m}$ (approximate for both terrain features), $\theta = 252 \text{ K}$, and $\Delta\theta = 3 \text{ K}$ gives $Fr = 1.85$. AMPS indicates wind speeds of approximately 50 m s^{-1} at 2300 UTC (Fig. 3) and AWS observations indicate wind speeds upward of 60 m s^{-1} at 2000 UTC and around 40 m s^{-1} at 2300 UTC (Fig. 2). Acceleration on the lee slope of Black Island indicates a downslope windstorm. Downslope windstorms are the result of vertically propagating large-amplitude mountain waves. The primary generation mechanism for downslope windstorms

is a transition of flow regimes at the top of the mountain, based on shallow-water hydraulic theory (Long 1953; Durran 1986). Hydraulic theory and the shallow-water model provide a simplified model for downslope windstorms, in that effects from a continuously stratified atmosphere and the vertical propagation of energy are neglected. Quantitative analysis of downslope effects is not permissible for this case because of the complex topography, variable upstream conditions, and the lack of upper-air observations. An idealized, high-resolution modeling study of downslope windstorms for the Ross Island region is beyond the scope of this paper. However, a qualitative analysis of AMPS output can provide insight into the role that downslope windstorms have in producing strong winds in the McMurdo area.

The acceleration of flow on the lee slope is the result of subcritical ($Fr < 1$) flow upstream of the obstacle transitioning to supercritical ($Fr > 1$) flow on the lee slope. In this case the application of the Froude number differs from that of a barrier wind diagnosis, where the ratio is a function of terrain height. Instead, the Froude number is applied to a hydraulic layer, which in this case is a stable layer underlying a less stable layer above. The Froude number can be defined as the ratio of fluid velocity to the propagation speed of shallow-water gravity waves. Because wave propagation speed is a function of fluid depth, the Froude number can be interpreted as the ratio of fluid velocity to layer depth:

$$Fr = \frac{u}{\sqrt{gD}}, \quad (6)$$

where u is the fluid velocity and D is the fluid thickness. Dynamically, the Froude number represents the ratio of the magnitude of nonlinear advection to the magnitude of the pressure gradient generated by changes in fluid depth (Durran 1990):

$$u \frac{\partial u}{\partial x} / g \frac{\partial D}{\partial x} = -Fr^2. \quad (7)$$

The shallow-water momentum equation,

$$u \frac{\partial u}{\partial x} + g \frac{\partial D}{\partial x} + g \frac{\partial h}{\partial x} = 0, \quad (8)$$

with the aid of the shallow-water continuity equation,

$$\frac{\partial uD}{\partial x} = 0, \quad (9)$$

can be rearranged to show that changes in the depth of the fluid depend on the Froude number and on the terrain height:

$$(1 - Fr^{-2}) \frac{\partial(D + h)}{\partial x} = \frac{\partial h}{\partial x}, \quad (10)$$

where h is the terrain height. With subcritical flow, and h increasing on the upslope, the fluid thickness will decrease (the quantity $D + h$ will decrease as well), and the shallow-water continuity equation dictates that the fluid velocity must increase. Integration of (8) results in

$$\frac{u^2}{2} + g(D + h) = 0, \quad (11)$$

which shows that the sum of kinetic energy (first term on lhs) and potential energy (second term on lhs) remain constant with the motion (Holton 1992). Therefore, for subcritical flow along the upslope (h increasing, D decreasing, $D + h$ decreasing, and u increasing), potential energy will be converted to kinetic energy. If the increase in fluid velocity and the decrease in thickness are sufficient to force the Froude number to exceed unity, the flow will become supercritical at the crest. Nonlinear effects will prevent the generation of a horizontal pressure gradient that is capable of decelerating the flow along the lee slope. Using (7) it can be shown that the fluid will continue to accelerate along the downslope as potential energy continues to be converted to kinetic energy.

Figure 15 shows the wave structure over Minna Bluff and Black Island based on the wind speed and vertical potential temperature distributions at 2100 UTC 15 May. The structure of the potential temperature and wind fields in Figs. 15 and 16 (taken 2 h later at 2300 UTC) show a qualitative resemblance to those seen in other observational and modeling studies of downslope windstorms, such as the 11 January 1972 Boulder windstorm (Klemp and Lilly 1975; Doyle et al. 2000) and those observed in the Mesoscale Alpine Programme (MAP) in the central Alps (Jiang and Doyle 2004). Common features include an upstream lower-tropospheric inversion layer, a downward-sloping potential temperature field on the lee slope, strong winds along the lee slope, and a hydraulic jump downstream of the topography. In Fig. 15, there is a stability interface located at an altitude of about 2 km upstream of Minna Bluff. Calculation of the Froude number within the hydraulic layer, as is done in idealized simulations, is not desirable for this case because the upstream stability and wind speed are not uniform in either space or time, terrain effects change with wind direction changes, and because of influences originating outside of the hydraulic layer. However, it is clear from a qualitative perspective that the depth of the fluid layer decreases on the upslope of Minna Bluff while the wind speed increases. On the downslope, acceleration con-

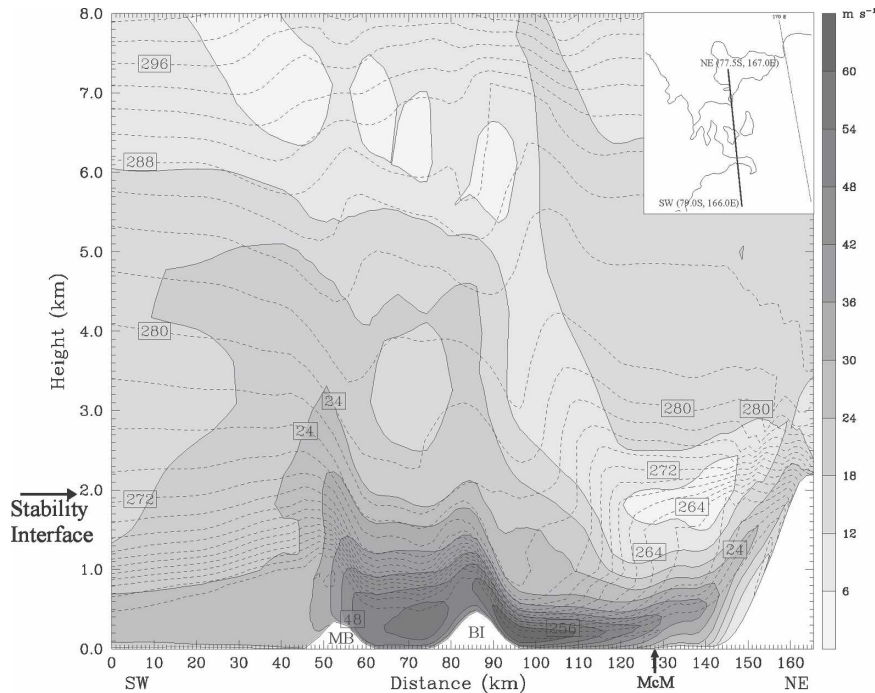


FIG. 15. Cross section of potential temperature (contoured, interval 2 K) and horizontal wind speed (shaded, interval 6 m s^{-1}) from -79.0°S , 166.0°E to -77.5°S , 167.0°E from AMPS 3.3-km grid at 2100 UTC 15 May 2004. MB represents Minna Bluff, BI represents Black Island, and McM represents McMurdo.

tinues, suggesting that flow has transitioned from subcritical to supercritical flow at the crest. The layer thickness has decreased to about 1.5 km. Figure 15 indicates that acceleration also occurs on the downslope of Black Island, although not to the extent as on the downslope of Minna Bluff. Downslope of Black Island the layer thickness has decreased to about 600 m. The core of maximum wind speeds extends about 30 km downstream of Black Island.

b. Alternative theories

Hydraulic theory fails to take into account energy propagation through the top of the hydraulic layer, which has led to alternative theories for the development of downslope windstorms. These theories involve reflection of upward-directed wave energy back toward the ground, leading to amplification of the wave system. Amplification can decrease the thickness of the hydraulic layer at the crest, leading to a transition to supercritical flow there. Klemp and Lilly (1975) show that upward-propagating linear gravity waves can be reflected downward from regions where the Scorer parameter changes rapidly. The downward-reflected waves can superimpose with the upward-propagating waves, leading to amplification, when there is a one-

half vertical wavelength shift between the ground and tropopause. The vertical wavelength is

$$\lambda_i \approx \frac{2\pi}{N_i} \frac{U_i + U_{i+1}}{2}, \quad (12)$$

where U and N are wind speed and Brunt–Väisälä frequency, respectively, for layer i . Using generalized values of $N = 0.02 \text{ s}^{-1}$ and $U = 25 \text{ m s}^{-1}$ for the bottom layer, $N = 0.01 \text{ s}^{-1}$ and $U = 15 \text{ m s}^{-1}$ for the top layer, and $U = 10 \text{ m s}^{-1}$ above the tropopause, the tropopause would need to be at an altitude of about 3.5 km for optimal superposition of waves. Therefore it is unlikely that reflection of linear gravity waves leads to wave amplification. Another possible wave amplification mechanism results from wave-breaking episodes (Clark and Peltier 1977, 1984; Peltier and Clark 1979, 1983; Clark and Farley 1984). “Wave-induced critical layers” are regions of mixing and reversed flow caused by breaking waves. Upward-propagating waves can reflect downward from a critical layer and amplify the wave system. Figure 15 shows a region of steep isentropes and weak flow at about 6-km altitude over the downslope of Black Island, indicative of wave-breaking there. Figure 16 shows that the wave-breaking region over the downslope of Black Island has descended to

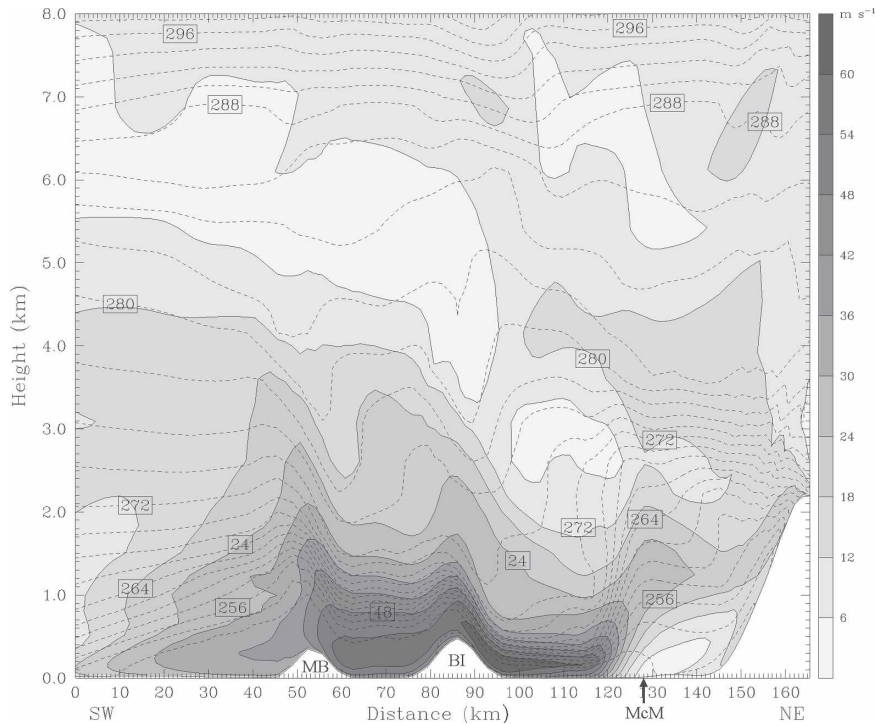


FIG. 16. Same as in Fig. 15 but for 2300 UTC 15 May 2004.

4.5 km and extends downward and downstream. These critical layers set up by wave breaking may lead to wave amplification over Black Island.

Figure 16 also shows a region downstream of Black Island, between the surface and 3-km altitude, where the isentropes rise steeply and the wind speeds decrease sharply within a distance of about 10 km. Along with strong upward vertical motion, these conditions are characteristic of a hydraulic jump. The hydraulic jump occurs as the flow transitions from supercritical flow to subcritical flow downstream of Black Island. Notice in Fig. 16 that the hydraulic jump is occurring upstream of McMURDO, so that the “shooting” flow from the downslope windstorm does not reach McMURDO. The upstream placement of the hydraulic jump is likely the reason that wind speeds are too low at McMURDO in AMPS.

6. AMPS errors

AMPS underestimates surface wind speed values in the McMURDO area, as forecasts of wind speed for McMURDO never exceed 25 m s^{-1} , when observed wind speeds at Arrival Heights are upward of 40 m s^{-1} and wind speeds at Williams Field and Pegasus North are upward of 30 m s^{-1} (Fig. 2). The microscale processes leading to differences in wind speeds between Mc-

MURDO area reporting sites cannot be resolved with AMPS or observations. However, it can be shown that mesoscale features in AMPS, supported by observations and previous studies, can infer the cause of underestimated wind speed forecasts in the McMURDO area.

The primary cause for the wind speed deficit in AMPS appears to result from a discrepancy in flow direction upstream of McMURDO. Throughout the strong wind event, wind directions at Minna Bluff are southwesterly in AMPS. As flow reaches Ross Island in AMPS, it is blocked and must flow around. Mass convergence leads to generation of a mesoscale pressure gradient and an associated deflection zone that is centered near McMURDO, as shown in Fig. 17. However, AWS observations show wind directions southerly to south-southwesterly at Minna Bluff, and as flow is blocked by Ross Island, a mesoscale high pressure region instead forms over Windless Bight, as shown in Slotten and Stearns (1987), O’Connor and Bromwich (1988), and Seefeldt et al. (2003). Unlike in AMPS, the deflection zone does not extend to McMURDO, so that flow will not split just upstream of there. The location of the hydraulic jump is collocated with the strong pressure gradient associated with the southern edge of the mesoscale high pressure region. Based on the hydraulic model discussed in section 5a, the pressure gradient

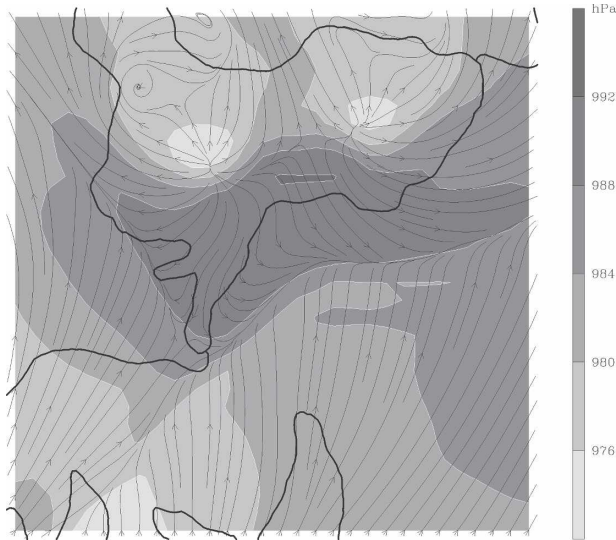


FIG. 17. Surface streamlines and sea level pressure (shaded, interval 4 hPa) from AMPS 3.3-km grid at 0000 UTC 16 May 2004.

acts to decelerate the wind by counterbalancing nonlinear advection. Without the mesoscale high pressure region upstream of Ross Island, deceleration by the horizontal pressure gradient cannot otherwise occur because changes in hydraulic layer thickness cannot generate a pressure gradient capable of counterbalancing nonlinear advection (Durrán 1986). The transition of flow regimes from supercritical to subcritical results in a turbulent hydraulic jump. As the pressure gradient shifts location, so does the hydraulic jump. Therefore in reality the hydraulic jump (and the downstream edge of the shooting flow) will shift northward, so that the downslope windstorm extends to McMurdo.

7. Conclusions and discussion

a. Event analysis and forecast assessment

The McMurdo 15–16 May 2004 windstorm originates from a lower-tropospheric cyclone tracking from the Siple Coast onto the Ross Ice Shelf. Easterly winds in the southern sector of the cyclone cannot traverse the Transantarctic Mountains, and a barrier wind develops, flowing northward. Wind speeds of 20–30 m s^{-1} along the western side of the cyclone are produced by southerly barrier winds. Cold air at the surface is entrained into the cyclone and barrier wind, setting up a large vertical temperature gradient just south of Ross Island by 1800 UTC 15 May. The strong low-level stability and high wind speeds result in downslope windstorms over Minna Bluff and Black Island that produce severe wind damage at McMurdo.

Downslope windstorms along the lee slopes of Minna Bluff, Black Island, and White Island appear to be common whenever there are southerly winds greater than about 15 m s^{-1} and when low-level inversion conditions are present. This case is unique in that the strong winds along the lee slopes propagate past the bottom of the lee slope. Maximum wind speeds over 70 m s^{-1} at McMurdo Building 71 and Arrival Heights appear to be caused by downslope effects off of local topographic features in the area (Observation Hill and Crater Hill). The low-level inversion caused by the shooting flow from the downslope windstorm off of Black Island would set up favorable conditions for additional downslope windstorms in the McMurdo area. However, a microscale observation network would be necessary to properly observe such effects.

AMPS is vital for diagnosing the physical processes involved in producing the windstorm at McMurdo. Errors in cyclone position and timing in AMPS lead to relatively minor biases at most AWS sites. The complex topography of the McMurdo area, along with the sensitivity of the mountain wave system to upstream conditions, cause errors to be amplified during the times of peak wind speeds. The amplification of errors, combined with important effects below the resolution of the model and observations, illustrate the challenges to numerical modeling present in this case study.

b. Model improvements and future research

As of this writing, AMPS is transitioning from the MM5 to the Weather Research and Forecasting model (WRF; Skamarock et al. 2005). The higher-order numerics of WRF, along with the increased resolution of the Ross Island grid in AMPS (3.3 to 2.2 km), should improve model representations of mesoscale features like mountain waves. Model errors away from areas of complex terrain appear to originate from inaccuracies in the storm track. Storm-track errors are likely caused by the limited observational coverage over continental Antarctica. A three-dimensional variational data assimilation (3DVAR) system (Barker et al. 2004) has since been implemented in the operational version of AMPS, and current research involving 3DVAR in the Advanced Research version of WRF shows great promise for improvements in the initial conditions for AMPS. Specifically for this event, Powers (2007) shows that the assimilation of filtered MODIS cloud-track winds in WRF AMPS improves the trajectory and timing of the synoptic-scale cyclone featured in this case compared with MM5 AMPS and WRF AMPS, leading to more realistic wind speed forecasts for the McMurdo area.

Several mesoscale effects illustrated in this study require further research. Barrier winds along the Transantarctic Mountains are often associated with the Ross Ice Shelf airstream (RAS; Parish et al. 2006). Analysis of the 15–16 May 2004 severe wind event in regard to the RAS has been done by Adams (2005). This study and future studies of the RAS will aid in placing this severe wind event in the proper synoptic-scale and climatological perspective. Although not necessarily poorly handled by AMPS, downslope windstorms in the Ross Island region require further study. The authors are not aware of any observational or modeling studies focused on downslope windstorms and the subsequent impact on McMurdo. A modeling study utilizing higher horizontal resolution could better analyze the effects of errors in background conditions on mountain wave representation. Increased resolution in the vertical would also be necessary to identify stratospheric wave-breaking events and their effects on wave formation.

Acknowledgments. This research is supported by the National Aeronautics and Space Administration (Grant NNG04GM26G) and the National Science Foundation, Office of Polar Programs (Grant 0230361 and UCAR Subcontract S01-22901). We thank the Italian Antarctic Program (Andrea Pellegrini) for providing additional AWS data, the Space and Naval Warfare Systems Center (Art Cayette and Bob Vehorn) for additional information on their AWS sites in the McMurdo area, and Andy Monaghan of BPRC/Ohio State for his logistical support throughout the project.

REFERENCES

- Adams, A. S., 2005: The relationship between topography and the Ross Ice Shelf air stream. Ph.D. dissertation, University of Wisconsin—Madison, 125 pp.
- Barker, D. M., W. Huang, Y.-R. Guo, A. J. Bourgeois, and Q. N. Xiao, 2004: A three-dimensional variational data assimilation system for MM5: Implementation and initial results. *Mon. Wea. Rev.*, **132**, 897–914.
- Bromwich, D. H., J. F. Carrasco, and C. R. Stearns, 1992: Satellite observations of katabatic-wind propagation for great distances across the Ross Ice Shelf. *Mon. Wea. Rev.*, **120**, 1940–1949.
- , J. J. Cassano, T. Klein, G. Heinemann, K. M. Hines, K. Steffen, and J. E. Box, 2001: Mesoscale modeling of katabatic winds over Greenland with the Polar MM5. *Mon. Wea. Rev.*, **129**, 2290–2309.
- , A. J. Monaghan, K. W. Manning, and J. G. Powers, 2005: Real-time forecasting for the Antarctic: An evaluation of the Antarctic Mesoscale Prediction System (AMPS). *Mon. Wea. Rev.*, **133**, 579–603.
- Cassano, J. J., J. E. Box, D. H. Bromwich, L. Li, and K. Steffen, 2001: Evaluation of Polar MM5 simulations of Greenland's atmospheric circulation. *J. Geophys. Res.*, **106**, 33 867–33 890.
- Clark, T. L., and W. R. Peltier, 1977: On the evolution and stability of finite-amplitude mountain waves. *J. Atmos. Sci.*, **34**, 1715–1730.
- , and R. D. Farley, 1984: Severe downslope windstorm calculations in two and three spatial dimensions using anelastic interactive grid nesting: A possible mechanism for gustiness. *J. Atmos. Sci.*, **41**, 329–350.
- , and W. R. Peltier, 1984: Critical level reflection and the resonant growth of nonlinear mountain waves. *J. Atmos. Sci.*, **41**, 3122–3134.
- Dalrymple, P., 2004: A wicked storm. *Antarctic Society Newsletter*, Vols. 4–5, No. 1, 7–10. [Available from Antarctic Society Newsletter, Box 325, Port Clyde, ME 04855.]
- Doyle, J. D., and Coauthors, 2000: An intercomparison of model-predicted wave breaking for the 11 January 1972 Boulder windstorm. *Mon. Wea. Rev.*, **128**, 901–914.
- Durrán, D. R., 1986: Another look at downslope windstorms. Part I: The development of analogs to supercritical flow in an infinitely deep, continuously stratified fluid. *J. Atmos. Sci.*, **43**, 2527–2543.
- , 1990: Mountain waves and downslope winds. *Atmospheric Processes over Complex Terrain*, Meteor. Monogr., No. 45, Amer. Meteor. Soc., 59–82.
- Grell, G. A., J. Dudhia, and D. R. Stauffer, 1995: A description of the fifth-generation Penn State/NCAR Mesoscale Model (MM5). NCAR Tech. Note NCAR/TN-398+STR, 122 pp.
- Guo, Z., D. H. Bromwich, and J. J. Cassano, 2003: Evaluation of Polar MM5 simulations of Antarctic atmospheric circulation. *Mon. Wea. Rev.*, **131**, 384–411.
- Haltiner, G. J., and R. T. Williams, 1980: *Numerical Prediction and Dynamic Meteorology*. 2nd ed. John Wiley & Sons, 477 pp.
- Holton, J. R., 1992: *An Introduction to Dynamic Meteorology*. 3rd ed. Academic Press, 511 pp.
- Jiang, Q., and J. D. Doyle, 2004: Gravity wave breaking over the central Alps: Role of complex terrain. *J. Atmos. Sci.*, **61**, 2249–2266.
- Klemp, J. B., and D. R. Lilly, 1975: The dynamics of wave-induced downslope winds. *J. Atmos. Sci.*, **32**, 320–339.
- Liu, Z., and D. H. Bromwich, 1993: Acoustic remote sensing of planetary boundary layer dynamics near Ross Island, Antarctica. *J. Appl. Meteor.*, **32**, 1867–1882.
- Long, R. R., 1953: Some aspects of the flow of stratified fluids I: A theoretical investigation. *Tellus*, **5**, 42–58.
- Nuss, W. A., and D. W. Tittley, 1994: Use of multiquadric interpolation for meteorological objective analysis. *Mon. Wea. Rev.*, **122**, 1611–1631.
- O'Connor, W. P., and D. H. Bromwich, 1988: Surface airflow around Windless Bight, Ross Island, Antarctica. *Quart. J. Roy. Meteor. Soc.*, **114**, 917–938.
- , —, and J. F. Carrasco, 1994: Cyclonically forced barrier winds along the Transantarctic Mountains near Ross Island. *Mon. Wea. Rev.*, **122**, 137–150.
- Parish, T. R., J. J. Cassano, and M. W. Seefeldt, 2006: Characteristics of the Ross Ice Shelf air stream as depicted in Antarctic Mesoscale Prediction System simulations. *J. Geophys. Res.*, **111**, D12109, doi:10.1029/2005JD006185.
- Peltier, W. R., and T. L. Clark, 1979: The evolution and stability of finite-amplitude mountain waves. Part II: Surface wave drag and severe downslope winds. *J. Atmos. Sci.*, **36**, 1498–1529.
- , and —, 1983: Nonlinear mountain waves in two and three spatial dimensions. *Quart. J. Roy. Meteor. Soc.*, **109**, 527–548.

- Powers, J. G., 2007: Numerical prediction of an Antarctic severe wind event with the Weather Research and Forecasting (WRF) model. *Mon. Wea. Rev.*, **135**, 3134–3157.
- , A. J. Monaghan, A. M. Cayette, D. H. Bromwich, Y.-H. Kuo, and K. W. Manning, 2003: Real-time mesoscale modeling over Antarctica: The Antarctic Mesoscale Prediction System. *Bull. Amer. Meteor. Soc.*, **84**, 1533–1545.
- Schwerdtfeger, W., 1984: *Weather and Climate of the Antarctic*. Elsevier, 261 pp.
- Seefeldt, M. W., G. J. Tripoli, and C. R. Stearns, 2003: A high-resolution numerical simulation of the wind flow in the Ross Island region, Antarctica. *Mon. Wea. Rev.*, **131**, 435–458.
- Skamarock, W. C., J. B. Klemp, J. Dudhia, D. O. Gill, D. M. Barker, W. Wang, and J. G. Powers, 2005: A description of the Advanced Research WRF version 2. NCAR Tech. Note NCAR/TN-468+STR, 88 pp.
- Slotten, H. R., and C. R. Stearns, 1987: Observations of the dynamics and kinematics of the atmospheric surface layer on the Ross Ice Shelf, Antarctica. *J. Climate Appl. Meteor.*, **26**, 1731–1745.
- Stearns, C. R., L. M. Keller, G. A. Weidner, and M. Sievers, 1993: Monthly mean climatic data for Antarctic automatic weather stations. *Antarctic Meteorology and Climatology: Studies Based on Automatic Weather Stations*, Antarctic Research Series, Vol. 61, D. H. Bromwich and C. R. Stearns, Eds., Amer. Geophys. Union, 1–21.

Copyright of *Monthly Weather Review* is the property of American Meteorological Society and its content may not be copied or emailed to multiple sites or posted to a listserv without the copyright holder's express written permission. However, users may print, download, or email articles for individual use.